Immersed boundary methods in wave-based virtual acoustics

Accepted for publication, Journal of the Acoustical Society of America, 21 February 2022.

After it is published, it will be found at `http://asa.scitation.org/journal/jas`

Immersed Boundary Methods in Wave-based Virtual Acoustics

Stefan Bilbao
Acoustics and Audio Group, University of Edinburgh
Room 2.10 Alison House, 12 Nicolson Square
Edinburgh, United Kingdom EH8 9DF[a)]

Volumetric wave-based simulation methods for room and virtual acoustics, such as the finite difference time domain method, are computationally intensive; for large volumes, operation over a regular grid is desirable for the sake of efficiency. In coping with realistic irregular geometries (such as enclosures or scattering objects), form-fitting meshing can disturb grid regularity and introduce new difficulties in terms of maintaining numerical stability. An alternative is the immersed boundary method, allowing for the representation of an irregular boundary over a regular grid through additional forcing terms in the dynamical system. While heavily used in fluid-structure interaction problems, such methods have seen less application in virtual acoustics. In this article, a simplified form of the immersed boundary method, tailored to virtual acoustics is presented. Under appropriate passivity-preserving discretisation techniques, simple numerical stability conditions can be proved, and in particular, impedance boundaries may be incorporated easily without any risk of numerical instability. In addition, the method retains a largely explicit character with a small linear system solution required over the immersed boundary surface. Numerical results in 2D and 3D, illustrating various interior and exterior problem scenarios are presented.

[https://doi.org(DOI number)]

[XYZ] Pages: 1–12

I. INTRODUCTION

Volumetric wave-based time domain methods are increasingly applied to large scale problems in room and virtual acoustics. While computationally intensive, finite difference time domain methods (FDTD)[1–3], finite volume time domain methods (FVTD)[4] and others[5–8] have been applied in realistic geometries, and over the full audio bandwidth[9]. Such methods offer, in theory, a complete solution to the problem of virtual acoustic emulation. Comparisons between methods can be made with respect to three inter-related attributes: a) *efficiency*, or the computation required, how it scales with problem size, and ease of parallelisation; b) *accuracy*, or how much numerical error is introduced, and c) *numerical stability*, and the possibility and difficulty of obtaining robust conditions. A major difficulty in virtual acoustics, in both algorithm design and implementation, is in coping with complex geometries, either for the enclosing space itself, or objects embedded within it. The choice of approach impacts upon all three attributes mentioned above.

For regular grid arrangements, preferred for large-scale algorithm parallelisation, a common approach is to employ a basic "staircasing" of a complex geometry[10]. See Figure 1 at left. When staircasing is employed within the basic nearest-neighbour FDTD method, numerical stability under the simple Courant-Friedrichs-Lewy (CFL) condition[11] may be easily proved. This holds even for general passive frequency-dependent boundary conditions[4]. A key drawback is that the temporal coherence of scattered waves is significantly disturbed in the high-frequency limit. (In addition, for enclosures, the surface area under staircasing is incorrect, even in the limit of small grid spacings, and decay times can be grossly incorrect[4].) When more accurate (and less local) simulation methods are used over regular grids (such as higher-order accurate FDTD[12], or Fourier spectral methods[5]), stability conditions become much more difficult to obtain under staircasing termination. One may need to perform eigenvalue checks for the update over the entire domain, a computationally intensive undertaking that may reveal instability without offering a remedy.

One solution is boundary-conforming meshing—this leads to a great increase in the accuracy of computed responses, in terms of calculated decay times, modal frequencies for enclosures, and also the coherence of temporal responses[4]. See Figure 1, middle. Flux conservation methods such as FVTD[4,13] achieve this in the simplest way, and this carries over to methods of the finite element[8] or spectral element[7] variety. But the computational domain as a whole becomes unstructured and less

a); sbilbao@ed.ac.uk

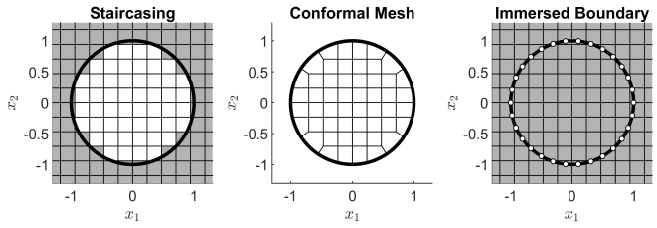

FIG. 1. A circular boundary in 2D under: staircasing termination (left), with "interior" cells indicated in white; conformal meshing (middle); and with an immersed boundary (right), with forcing locations indicated as white dots.

amenable to parallelisation, and, for explicit methods, new stability considerations arise, dependent on mesh geometry, again requiring global eigenvalue checks. Meshing itself, carried out prior to run time, can become computationally prohibitive, and there are new storage considerations to hold the connectivity graph of any resulting unstructured mesh. One means of avoiding such difficulties is to employ Cartesian cut-cell techniques[14], retaining a regular grid ordering (with some alterations if merging techniques[15] are employed); but even here, the problem of small residual cell-sizes and its influence on stability conditions remains a large unsolved problem[15].

In applications involving fluid-structure interactions, one approach to avoiding meshing of a boundary surface is through the use of immersed boundary techniques[16–19]. (including other related techniques such as the immersed interface method[10] and volume penalisation methods[20].) See Figure 1, at right. Here, the boundary itself is replaced by a forcing term in the underlying dynamical system. If a regular computational grid is used, parallelisation is undisturbed, which is ideal in the context of large-scale virtual acoustics, where operation in parallel hardware will be necessary for the foreseeable future.

In virtual acoustics, the defining equations (usually the acoustic wave equation) are simpler than in general fluids[21–23] or nonlinear acoustics[24,25] applications, and boundaries are normally immobile. There are thus opportunities for simplified algorithm design, allowing efficient operation over regular grids, and yielding simple global numerical stability conditions through an energy-based or passivity criterion. New features to be examined in the context of virtual acoustics include the accuracy of modal frequency calculations for enclosed spaces, the effects of rotation of an object relative to the underlying Cartesian grid, and leakage through immersed boundaries, particularly over long time scales. In addition, despite the avoidance of form-fitting meshing and the desirable attribute of operation over regular grids, there are new computational costs to consider, and particularly the partially-implicit behaviour of such methods over the immersed boundary. New numerical design choices emerge, including the density of the representation of the continuous forcing and the type of interpolation employed, that need to be addressed in the context of virtual acoustics.

The immersed boundary is introduced in the continuous framework in Section II, alongside a characterisation of impedance conditions for an enclosed boundary. The fully discrete FDTD scheme for the acoustic field is introduced in Section III, alongside a family of interpolants, and the complete algorithm design for an immersed boundary. Numerical examples in 2D and 3D, simulating both exterior and interior geometries, and illustrating some of the features mentioned above are presented in Section IV. The focus of the examples will be mainly on the important baseline case of the rigid boundary, or Neumann condition, of central importance in room and virtual acoustics. Following concluding remarks in Section V, a complete stability analysis of FDTD with an immersed boundary, drawing upon the notion of discrete passivity, is given in Appendix A.

II. IMMERSED BOUNDARY METHODS

The defining equations of linear acoustics in d dimensions may be written in conservation form as:

$$\frac{1}{\rho c^2}\partial_t p + \nabla \cdot \mathbf{v} = u_{\text{in}}\delta^{(d)}\left(\mathbf{x}-\mathbf{x}_{\text{in}}\right) \qquad \rho\partial_t \mathbf{v} + \nabla p = \mathbf{0}\,. \tag{1}$$

Here, $p(\mathbf{x},t)$ is the acoustic pressure, in kg$\cdot$ m^{2-d} $\cdot$ s^{-2} and $\mathbf{v}(\mathbf{x},t) = [v_1,\ldots,v_d]$ is the d-dimensional particle velocity, in m$\cdot$ s^{-1}. Both are functions of $\mathbf{x} = [x_1,\ldots,x_d] \in \mathcal{V} \subset \mathbb{R}^d$ and time $t \in \mathbb{R}$. ρ is density in kg$\cdot$ m^{-d} and c is the wave speed in m$\cdot$ s^{-1}. ∂_t represents partial differentiation with respect to t, and ∇ is the d-dimensional gradient operation, defined by $\nabla = [\partial_{x_1},\ldots,\partial_{x_d}]$, with $\nabla\cdot$ the associated divergence. Here, d will be set to $2, 3$.

Initial conditions are assumed quiescent; the system is driven by a point source of strength $u_{\text{in}} = u_{\text{in}}(t)$, in m^d $\cdot$ s^{-1}, where $\delta^{(d)}$ represents a d-dimensional spatial Dirac delta function, selecting the driving location $\mathbf{x} = \mathbf{x}_{\text{in}}$. More general directional[26,27] source models could be included here but are not relevant to the current study of scattering in the interior of a given domain. For the same reason, the domain $\mathcal{V}$ is assumed to be infinite or periodic, so boundary conditions need not be considered (though in the simulations in Section IV, a simple absorbing boundary condition is employed).

Equations (1) may be consolidated to the familiar d-dimensional second order wave equation, here with a forcing term, and using the Laplacian operator $\Delta = \nabla\cdot\nabla$:

$$\frac{1}{c^2}\partial_t^2 p - \Delta p = \rho\frac{du_{\text{in}}}{dt}\delta^{(d)}\left(\mathbf{x}-\mathbf{x}_{\text{in}}\right)\,. \tag{2}$$

System (1) satisfies an energy balance of the form

$$\frac{dE_{\text{ac}}}{dt} = P_{\text{in}} \qquad E_{\text{ac}} = \int_{\mathcal{V}} \frac{p^2}{2\rho c^2} + \frac{\rho|\mathbf{v}|^2}{2} d\mathbf{x}\,, \tag{3}$$

where $E_{\text{ac}} = E_{\text{ac}}(t)$ is the total acoustic field energy in J, and where $P_{\text{in}} = p(\mathbf{x}_{\text{in}},t)u_{\text{in}}(t)$ is input power due to the driving term.

A. Immersed Boundary

Assume a $(d-1)$-dimensional surface Ω internal to the region $\mathcal{V}$, and of volume $|\Omega|$. Associated with each point $\boldsymbol{\xi} \in \Omega$ over the surface is a normal vector $\mathbf{n}(\boldsymbol{\xi}) \in \mathbb{R}^d$. See Figure 2. An immersed boundary may then be added to the second of system (1) as

$$\rho \partial_t \mathbf{v} + \nabla p = \int_\Omega \mathbf{n}(\boldsymbol{\xi}) p^*(\boldsymbol{\xi}, t) \delta^{(d)}(\mathbf{x} - \boldsymbol{\xi})\, d\sigma\,. \tag{4}$$

Here, $p^*(\boldsymbol{\xi}, t)$ is a distributed forcing term, acting normal to the surface. The forcing function p^* is related back to the normal fluid velocity $v^*(\boldsymbol{\xi}, t) = \mathbf{n}(\boldsymbol{\xi}) \cdot \mathbf{v}(\boldsymbol{\xi}, t)$ over the boundary surface Ω, or as

$$v^*(\boldsymbol{\xi}, t) = \mathbf{n}(\boldsymbol{\xi}) \cdot \int_\mathcal{V} \mathbf{v}(\mathbf{x}) \delta^{(d)}(\mathbf{x} - \boldsymbol{\xi})\, d\mathbf{x} \qquad \boldsymbol{\xi} \in \Omega\,. \tag{5}$$

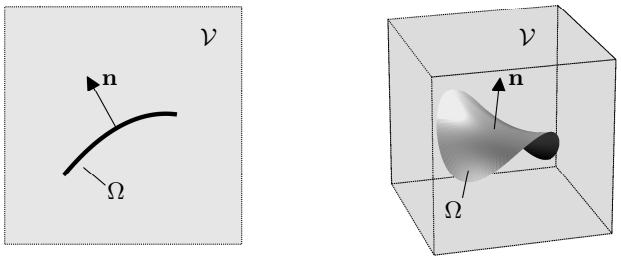

FIG. 2. The domain $\mathcal{V}$, and an immersed boundary Ω with normal $\mathbf{n}$, in 2D (left) and 3D (right).

In acoustics applications, one possible representation of such a forcing is through an impedance relationship:

$$\hat{p}^*(\boldsymbol{\xi}, s) = -Z_0 \zeta(\boldsymbol{\xi}, s) \hat{v}^*(\boldsymbol{\xi}, s)\,, \tag{6}$$

written in terms of Laplace-transformed pressure $\hat{p}^*(\boldsymbol{\xi}, s)$ and velocity $\hat{v}^*(\boldsymbol{\xi}, s)$. Here, $Z_0 = \rho c$ is the characteristic impedance of air, and $\zeta(\boldsymbol{\xi}, s)$ is a normalized impedance function. ζ is constrained to be passive, or a positive real function[28] of complex frequency s for all $\boldsymbol{\xi} \in \Omega$:

$$\mathrm{Re}(\zeta(\boldsymbol{\xi}, s)) \geq 0 \qquad \text{when} \qquad \mathrm{Re}(s) > 0\,. \tag{7}$$

As an example, consider the particular choice of

$$\zeta(\boldsymbol{\xi}, s) = R + Ms + \frac{K}{s} \qquad R, M, K \geq 0\,. \tag{8}$$

In the time domain, the representation of Goldstein[17] follows (under the simplification $M = 0$):

$$p^* = -Z_0 \left(R v^* + M \partial_t v^* + K \int_t v^* dt' \right)\,. \tag{9}$$

This formulation differs from usual immersed boundary in that it is framed in terms of the normal component of the velocity only, allowing an alignment with the notion of an acoustical impedance. It also differs in the sense that the boundary also may behave as an acoustical barrier, capable of transmitting energy.

B. Discrete Forcing

As a preparatory step, prior to full discretisation, one may approximate the continuous immersed boundary (4) by a finite set of V forcing terms, as

$$\rho \partial_t \mathbf{v} + \nabla p = \sum_{\nu=1}^{V} \mathbf{n}_\nu p^*_\nu(t) \delta^{(d)}(\mathbf{x} - \boldsymbol{\xi}_\nu)\, \Delta\sigma_\nu\,. \tag{10}$$

The forcing pressure p^*_ν, $\nu = 1, \ldots, V$, acts at $\mathbf{x} = \boldsymbol{\xi}_\nu$, and in direction $\mathbf{n}_\nu$ over a surface patch of $(d-1)$-dimensional volume $\Delta\sigma_\nu$. It is assumed that the patch volumes cover Ω such that $\sum_{\nu=1}^{V} \Delta\sigma_\nu = |\Omega|$. The finite set of forcing pressures p^*_ν may be related to interpolated field velocities (5) in the Laplace domain by discretising (6) as:

$$\hat{p}^*_\nu(s) = -Z_0 \zeta_\nu(s) \hat{v}^*_\nu(s) \qquad \nu = 1, \ldots, V \tag{11}$$

for positive real impedances $\zeta_\nu(s)$, where the interpolated field velocities are given by

$$v^*_\nu(t) = \mathbf{n}_\nu \cdot \int_\mathcal{V} \mathbf{v}(\mathbf{x}, t) \delta^{(d)}(\mathbf{x} - \boldsymbol{\xi}_\nu)\, d\mathbf{x} \qquad \nu = 1, \ldots, V\,. \tag{12}$$

If the local impedances $\zeta(\boldsymbol{\xi}, s)$ are positive real, then the system as a whole is passive. When a concrete realisation of the impedance is available, this may be demonstrated directly in the time domain. Taking the simple case of the series impedance given by (8), one has the following generalisation of the energy balance (3):

$$\frac{d}{dt}\left(E_\mathrm{ac} + E_b\right) = P_\mathrm{in} - Q_\mathrm{b}\,, \tag{13}$$

where

$$E_\mathrm{b} = \frac{Z_0}{2} \sum_{\nu=1}^{V} \left(M_\nu \left(v^*_\nu\right)^2 + K_\nu \left(g^*_\nu\right)^2 \right) \Delta\sigma_\nu \geq 0 \tag{14a}$$

$$Q_\mathrm{b} = Z_0 \sum_{\nu=1}^{V} R_\nu \left(v^*_\nu\right)^2 \Delta\sigma_\nu \geq 0 \tag{14b}$$

and where $dg^*_\nu/dt = v^*_\nu$. Under unforced conditions, and due to the non-negativity of E_ac, E_b and Q_b, the system is dissipative as a whole, and lossless when $R_\nu = 0$.

III. DISCRETISATION

For the purposes of this investigation, we employ the most basic discretisation possible. The standard interleaved form of FDTD, as used by many authors in acoustics applications[2], is descended from techniques used in electromagnetic field simulation[29].

A. Grids and Grid Functions

Assume a spatial grid spacing X and time step T. As the dual variables p and $\mathbf{v}$ will be approximated by interleaved grid functions, it is helpful to adopt the following simplified indexing strategy.

The grid function $p^n_{\mathbf{q}}$, for integer n and an integer-valued d-vector $\mathbf{q} = [q_1, \ldots, q_d] \in \mathcal{B} \subset \mathbb{Z}^d$, is an approximation to $p(\mathbf{x}, t)$ at $t = nT$ and $\mathbf{x} = \mathbf{q}X$. The grid function $\mathbf{v}^{n+1/2}_{\mathbf{q}}$ is defined as $\mathbf{v}^{n+1/2}_{\mathbf{q}} = [v^{n+1/2}_{1,\mathbf{q}}, \ldots, v^{n+1/2}_{d,\mathbf{q}}]$. The ηth component $v^{n+1/2}_{\eta,\mathbf{q}}$ of this vector, $\eta = 1, \ldots, d$, is an approximation to $v_\eta(\mathbf{x}, t)$ at $t = (n+1/2)T$, and at the interleaved location $\mathbf{x} = (\mathbf{q} - (1/2)\mathbf{e}_\eta)X$, where $\mathbf{e}_\eta$ is a unit vector in direction x_η. For a given $\mathbf{q}$, the spatial locations of $p^n_{\mathbf{q}}$ and $\mathbf{v}^{n+1/2}_{\mathbf{q}}$ form a simplex, as illustrated in Figure 3. Note that for simplicity of notation and analysis purposes, we assume here $\mathbf{q} \in \mathcal{B}$ for both the pressure and velocity components—this assumption is true for an infinite or d-periodic domain, but must be modified for a finite domain with nontrivial outer boundary conditions.

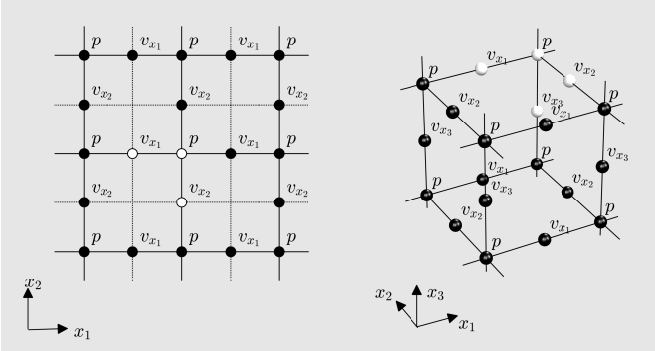

FIG. 3. Computational grids for FDTD in 2D (left) and 3D (right). The simplex of points sharing the same grid index is illustrated as a set of white points in either case.

B. Basic FDTD Scheme

Basic time difference operators D^+_t and D^-_t may be defined, through their action on a grid function $w^n_{\mathbf{q}}$, as

$$D^+_t w^n_{\mathbf{q}} = \frac{1}{T}\left(w^{n+1}_{\mathbf{q}} - w^n_{\mathbf{q}}\right) \qquad D^-_t w^n_{\mathbf{q}} = \frac{1}{T}\left(w^n_{\mathbf{q}} - w^{n-1}_{\mathbf{q}}\right). \tag{15}$$

Both approximate a first time derivative ∂_t. Also important is the two-point averaging operator μ^-_t, defined as

$$\mu^-_t w^n_{\mathbf{q}} = \frac{1}{2}\left(w^n_{\mathbf{q}} + w^{n-1}_{\mathbf{q}}\right). \tag{16}$$

These definitions hold when n is an integer or half integer.

Similarly, approximations to a spatial derivative ∂_{x_η}, $\eta = 1, \ldots, d$, may be written as D^+_η and D^-_η, and act as

$$D^+_\eta w^n_{\mathbf{q}} = \frac{1}{X}\left(w^n_{\mathbf{q}+\mathbf{e}_\eta} - w^n_{\mathbf{q}}\right) \quad D^-_\eta w^n_{\mathbf{q}} = \frac{1}{X}\left(w^n_{\mathbf{q}} - w^n_{\mathbf{q}-\mathbf{e}_\eta}\right). \tag{17}$$

Forward and backward approximations D^+_∇ and D^-_∇ to the gradient operation may then be defined as

$$D^\pm_\nabla = [D^\pm_1, \ldots, D^\pm_d]. \tag{18}$$

A scheme for system (1), in the absence of a forcing term, may be written directly as

$$\frac{1}{\rho c^2} D^+_t p^n_{\mathbf{q}} + D^+_\nabla \cdot \mathbf{v}^{n+1/2}_{\mathbf{q}} = 0 \qquad \rho D^-_t \mathbf{v}^{n+1/2}_{\mathbf{q}} + D^-_\nabla p^n_{\mathbf{q}} = \mathbf{0}. \tag{19}$$

This is identical to Botteldooren's formulation of FDTD in acoustics[2]. When combined, this system of two updates results in the familiar two-step update approximating the unforced scalar second order equation (2) directly:

$$\frac{1}{c^2} D^+_t D^-_t p^n_{\mathbf{q}} - D_\Delta p^n_{\mathbf{q}} = 0. \tag{20}$$

Here, $D_\Delta = D^+_\nabla \cdot D^-_\nabla$ approximates the Laplacian Δ, and has the usual 5-point (in 2D) or 7-point (in 3D) stencil.

This is the simplest possible scheme for the wave equation, and by no means the best, particularly in terms of numerical dispersion artefacts. Superior schemes are available, often written for the second order system[3,12,30], but lacking a first-order form (that is, the Laplacian approximation may not be factorizable into separate divergence and gradient operations, and thus the immersed boundary approach is less suitable in these cases).

C. Interpolants

Approximations to the Dirac delta function at non-grid locations arise both in velocity interpolation in (5), and in the point forcing representation in (10). They also arise in the discrete representation of the source in (1) and, though not discussed here, in readout of a waveform from the computed field at an arbitrary location.

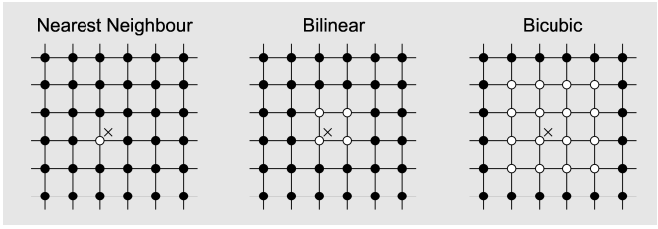

FIG. 4. Grid points, in white, included in forming nearest neighbour (left), bilinear (middle) and bicubic (right) interpolants or approximations to a Dirac delta function in 2D. The non-grid interpolation location is indicated as a cross.

In immersed boundary methods, various smoothing kernels are employed[19], as well as bi(tri)linear interpolation[18]. Assume first a forcing location $\mathbf{x}' \in \mathcal{V}$. An approximation to the Dirac delta function $\delta^{(d)}(\mathbf{x} - \mathbf{x}')$ over a grid indexed by $\mathbf{q} \in \mathcal{B}$ may be represented as

$$\frac{1}{X^d} J_{\mathbf{q}}(\mathbf{x}') \approxeq \delta^{(d)}(\mathbf{x} - \mathbf{x}'). \tag{21}$$

Here, the dimensionless grid function $J_{\mathbf{q}}(\mathbf{x}')$ selects $\mathbf{x} = \mathbf{x}'$ and must satisfy the basic moment condition[31,32] that $\sum_{\mathbf{q}\in\mathcal{B}} J_{\mathbf{q}}(\mathbf{x}') = 1$. This condition is satisfied by nearest-neighbour, bi(tri)linear and bi(tri)cubic approximations,

the choices that will be employed here. See Figure 4. A detailed investigation of interpolation design in 3D virtual acoustics has appeared recently[33].

In an interleaved setting, with the uniform indexing strategy adopted here, care must be taken as the index $\mathbf{q}$ refers to distinct locations in the case of all $d+1$ pressure/velocity field components. An approximation to the Dirac delta function may be immediately employed as an interpolant. For example, if the grid function $b_{\mathbf{q}}$ approximates the continuous function $b(\mathbf{x})$, then an interpolated approximation to $b(\mathbf{x}')$ follows from $\sum_{\mathbf{q}\in\mathcal{B}} J_{\mathbf{q}}(\mathbf{x}')b_{\mathbf{q}}$.

D. Discrete Immersed Boundary

First, (19) may be extended to include a source term, acting at $\mathbf{x}=\mathbf{x}_{\text{in}}$, according to (1), as

$$\frac{1}{\rho c^2}D_t^+ p_{\mathbf{q}}^n + D_\nabla^+ \cdot \mathbf{v}_{\mathbf{q}}^{n+1/2} = u_{\text{in}}^{n+1/2}\frac{1}{X^d}J_{\mathbf{q}}(\mathbf{x}_{\text{in}})\,. \tag{22}$$

Here $(1/X^d)J_{\mathbf{q}}(\mathbf{x}_{\text{in}})$ is some approximation to $\delta(\mathbf{x}-\mathbf{x}_{\text{in}})$, and $u_{\text{in}}^{n+1/2}$ is an approximation to the driving term $u_{\text{in}}(t)$ at $t=(n+1/2)T$ (perhaps arrived at through sampling).

Similarly, the second of (19) may be extended to include discrete boundary forcing, through an approximation to (10). For the ηth velocity component, one has:

$$\rho D_t^- v_{\eta,\mathbf{q}}^{n+1/2} + D_\eta^- p_{\mathbf{q}}^n = \sum_{\nu=1}^{V}\frac{n_{\eta,\nu}\Delta\sigma_\nu}{X^d}\mu_t^- p_\nu^{*,n+1/2}J_{\eta,\mathbf{q}}(\boldsymbol{\xi}_\nu)\,. \tag{23}$$

Here, $n_{\eta,\nu}$ is the ηth component of the νth normal vector $\mathbf{n}_\nu=[n_{1,\nu},\ldots,n_{d,\nu}]$.The grid function $J_{\eta,\mathbf{q}}(\boldsymbol{\xi}_\nu)/X^d$ is an approximation to a Dirac delta function over the ηth interleaved grid. Finally, $p_\nu^{*,n+1/2}$ is a discrete time approximation to $p_\nu^*(t)$, at $t=(n+1/2)T$, and thus temporally aligned with the velocity grid functions. Centering is achieved through the use of the two point averaging operator μ_t^- as defined in (16).

The discrete pressures $p_\nu^{*,n+1/2}$ will be related to interpolated values $v_\nu^{*,n+1/2}$ drawn from the velocity field through an impedance relationship approximating (11). The values $v_\nu^{*,n+1/2}$ follow from an approximation to (12):

$$v_\nu^{*,n+1/2} = \sum_{\eta=1}^{d} n_{\eta,\nu}\sum_{\mathbf{q}\in\mathcal{B}} J_{\eta,\mathbf{q}}(\boldsymbol{\xi}_\nu)v_{\eta,\mathbf{q}}^{n+1/2}\,. \tag{24}$$

Here the same grid function $J_{\eta,\mathbf{q}}(\boldsymbol{\xi}_\nu)$ used in (23) is now used as an interpolant. The use of such an adjoint has been pointed out by various authors[17], and is crucial to the analysis of numerical stability. See Appendix A.

E. Discrete-time Impedance Relationship

Returning to the continuous-time impedance relationship between $p_\nu^*(t)$ and $v_\nu^*(t)$ given in (11), we first assume that the normalized impedance $\zeta_\nu(s)$ may be expressed as a rational function as

$$\zeta_\nu(s) = \frac{\sum_{l=0}^{\tau_\nu} b_\nu^{(l)} s^l}{\sum_{l=0}^{\upsilon_\nu} a_\nu^{(l)} s^l} \tag{25}$$

for some finite polynomial orders τ_ν and υ_ν, $\nu=1,\ldots,V$. In the time domain, this implies the following differential relationship between $p_\nu^*(t)$ and $v_\nu^*(t)$:

$$\sum_{l=0}^{\upsilon_\nu} a_\nu^{(l)}\frac{d^l}{dt^l}p_\nu^* = -Z_0\sum_{l=0}^{\tau_\nu} b_\nu^{(l)}\frac{d^l}{dt^l}v_\nu^*\,. \tag{26}$$

In order to arrive at a discrete-time approximation, define first the trapezoidal differentiation operator

$$D_t^\circ = (\mu_t^-)^{-1}D_t^-\,, \tag{27}$$

where here, $(\mu_t^-)^{-1}$ is interpreted as the operator inverse of the two-point averaging operator μ_t^- as defined in (16). Under the discretisation rule $d/dt\to D_t^\circ$, the following discrete time recursion results:

$$\sum_{l=0}^{\upsilon_\nu} a_\nu^{(l)}(D_t^\circ)^l p_\nu^{*,n+1/2} = -Z_0\sum_{l=0}^{\tau_\nu} b_\nu^{(l)}(D_t^\circ)^l v_\nu^{*,n+1/2}\,. \tag{28}$$

This may be written, ultimately, as

$$p_\nu^{*,n+1/2} = -Z_0\gamma_\nu v_\nu^{*,n+1/2} + \Xi_\nu^{n+1/2} \tag{29}$$

for some constants $\gamma_\nu\geq 0$, where $\Xi_\nu^{n+1/2}$ includes previously computed values of p_ν^* and v_ν^*.

The approach here is similar to that presented in the case of boundary impedances in the FVTD setting[34]; in particular, the choice of the approximation (27) is passivity-preserving, and corresponds, in the frequency domain, to a bilinear transformation, allowing for a greatly simplified stability analysis. See Appendix A.

F. Complete Update

It is useful, for implementation purposes, to rewrite the entire update, including the source and immersed boundary, in a matrix-vector form. To this end, we assume that grid function $p_{\mathbf{q}}^n$ is consolidated into a $N_p\times 1$ vector $\mathbf{p}^n$, where N_p is the number of pressure grid locations in the discrete domain $\mathcal{B}$. Similarly, the d velocity component grid functions $v_{\eta,\mathbf{q}}^{n+1/2}$, $\eta=1,\ldots,d$, are consolidated into an $N_v\times 1$ vector $\mathbf{v}^{n+1/2}$. For (22), we have:

$$\frac{1}{\rho c^2}D_t^+\mathbf{p}^n + \mathbf{D}\mathbf{v}^{n+1/2} = u_{\text{in}}^{n+1/2}\frac{1}{X^d}\mathbf{j}_{\text{in}}\,, \tag{30a}$$

where the $N_p\times N_v$ matrix $\mathbf{D}$ represents the divergence operation $D_\nabla^+\cdot$, and the $N_p\times 1$ vector $\mathbf{j}_{\text{in}}$ encodes the spatial source distribution $J_{\mathbf{q}}(\mathbf{x}_{\text{in}})$. Similarly, the velocity updates (23) may be written as

$$\rho D_t^-\mathbf{v}^{n+1/2} - \mathbf{D}^T\mathbf{p}^n = \frac{1}{X^d}\mathbf{N}\mathbf{S}\left(\mu_t^-\mathbf{p}^{*,n+1/2}\right)\,. \tag{30b}$$

The V discrete forcing pressures $p_\nu^{*,n+1/2}$, $\nu=1,\ldots,V$ have been written as the $V\times 1$ vector $\mathbf{p}^{*,n+1/2}$. Here, the

$N_v \times N_p$ matrix $-\mathbf{D}^T$ represents the gradient operation D_∇^-. $\mathbf{S}$ is a $V \times V$ matrix with the values $\Delta\sigma_\nu$, $\nu = 1, \ldots, V$ on the diagonal. Finally, the $N_v \times V$ matrix $\mathbf{N}$ consolidates the V Dirac delta approximations, as well as the V normal directions.

Alongside $\mathbf{p}^{*,n+1/2}$, the set of interpolated velocity values $v_\nu^{*,n+1/2}$, $\nu = 1, \ldots, V$, may be consolidated into the $V \times 1$ vector $\mathbf{v}^{*,n+1/2}$, retrieved from the velocity field $\mathbf{v}^{n+1/2}$, according to (24), as

$$\mathbf{v}^{*,n+1/2} = \mathbf{N}^T \mathbf{v}^{n+1/2} \,. \tag{30c}$$

Finally, (29) may be written as

$$\mathbf{p}^{*,N+1/2} = -Z_0 \mathbf{\Gamma} \mathbf{v}^{*,n+1/2} + \mathbf{\Xi}^{n+1/2} \tag{30d}$$

for the $V \times V$ diagonal matrix $\mathbf{\Gamma}$ with γ_ν, $\nu = 1, \ldots, V$ on the diagonal, and the $V \times 1$ vector $\mathbf{\Xi}^{n+1/2}$, consisting of $\Xi_\nu^{n+1/2}$, $\nu = 1, \ldots, V$.

Equations (30a)–(30d), alongside the auxiliary calculation of $\mathbf{\Xi}^{n+1/2}$, constitute a complete update for the immersed boundary. (30a) is fully explicit: $\mathbf{p}^{n+1}$ may be computed directly from $\mathbf{p}^n$ and $\mathbf{v}^{n+1/2}$. The updates (30b)–(30d) may be combined into a single update for $\mathbf{v}^{n+1/2}$ of the form

$$\underbrace{\left(\mathbf{I}_{N_v} + \mathbf{W}\mathbf{W}^T\right)}_{\mathbf{A}} \mathbf{v}^{n+1/2} = \mathbf{q}^n \,, \tag{31}$$

where here $\mathbf{I}_{N_v}$ is the identity matrix of size $N_v \times N_v$, and $\mathbf{W}$ is an $N_v \times V$ matrix defined by $\mathbf{W} = \sqrt{cT/2X^d}\mathbf{N}\mathbf{S}^{1/2}\mathbf{\Gamma}^{1/2}$. $\mathbf{q}^n$ consists of previously computed (known) values of $\mathbf{p}$ and $\mathbf{v}$ up through time step n. Thus a linear system solution is required, involving the matrix $\mathbf{A}$. Notice, however, that a) it is strictly positive definite by construction and thus definitely invertible, and b) consists of a rank V perturbation of the identity matrix. Thus, using Sherman-Morrison inversion[35],

$$\mathbf{A}^{-1} = \mathbf{I}_{N_v} - \mathbf{W}\left(\mathbf{I}_V + \mathbf{W}^T\mathbf{W}\right)^{-1}\mathbf{W}^T \tag{32}$$

where $\mathbf{I}_V$ is a $V \times V$ identity matrix. Thus a linear system solution of size V is required, scaling with the number of boundary forcing points. Notice in particular that $\mathbf{W}$ is sparse, with each column containing non-zero values of the interpolant corresponding to a single forcing location. $\mathbf{W}^T\mathbf{W}$ will also be sparse, with a bandwidth depending on the width of the interpolant chosen, and the density of forcing locations relative to the grid spacing.

G. Special Cases

As a useful special case, consider the series impedance as given in (8). For this concrete realisation, it is possible to show that an energy balance exists, mirroring (13) for the continuous system:

$$D_t^+\left(\mathcal{E}_{\text{ac}} + \mathcal{E}_{\text{b}}\right) = \mathcal{P}_{\text{in}} - \mathcal{Q}_{\text{b}} \,, \tag{33}$$

where, with reference to the vector/matrix form given in Section III F,

$$\mathcal{E}_{\text{ac}} = \frac{\rho X^d}{2}|\mathbf{v}^{n-\frac{1}{2}}|^2 + \frac{X^d}{2\rho c^2}\left(\mathbf{p}^n\right)^T\mathbf{p}^{n-1} \tag{34}$$

$$\mathcal{E}_{\text{b}} = \frac{Z_0}{2}\left(|(\mathbf{SM})^{\frac{1}{2}}\mathbf{v}^{*,n-\frac{1}{2}}|^2 + |(\mathbf{SK})^{\frac{1}{2}}\mathbf{g}^{*,n-\frac{1}{2}}|^2\right) \geq 0$$

$$\mathcal{P}_{\text{in}} = \mu_t^- u_{\text{in}}^{n+\frac{1}{2}}\mathbf{j}_{\text{in}}^T\mathbf{p}^n$$

$$\mathcal{Q}_{\text{b}} = Z_0|(\mathbf{SR})^{\frac{1}{2}}\mu_t^-\mathbf{v}^{*,n+\frac{1}{2}}|^2 \geq 0$$

where here, $D_t^-\mathbf{g}^* = \mu_t^-\mathbf{v}^*$, and $\mathbf{R}$, $\mathbf{M}$ and $\mathbf{K}$ are $V \times V$ matrices with the values R_ν, M_ν and K_ν on their diagonals, respectively. The stored and dissipated energy terms corresponding to the immersed boundary, $\mathcal{E}_{\text{b}}$ and $\mathcal{Q}_{\text{b}}$ are both non-negative, and thus the system is strictly dissipative if $\mathcal{E}_{\text{ac}}$ is also non-negative; not shown here is that this is true under the CFL condition $cT/X \leq \sqrt{1/d}$. But the presence of the immersed boundary does not affect this stability condition. This property can be extended to fully general passive immersed boundaries, without a concrete realisation—see Appendix A.

As a further useful simplification, consider the case of a purely inertial immersed boundary with $R_\nu = K_\nu = 0$. In this case, $\mu_t^-\mathbf{p}^{*,n+\frac{1}{2}} = -Z_0\mathbf{M}D_t^-\mathbf{v}^{*,n+\frac{1}{2}}$. The updates (30a)–(30c) may now be combined into a single second order update in the pressure variable $\mathbf{p}$ alone:

$$\frac{1}{c^2}D_t^+D_t^-\mathbf{p}^n + \mathbf{D}\left(\mathbf{I}_{N_v} + \mathbf{Q}\mathbf{Q}^T\right)^{-1}\mathbf{D}^T\mathbf{p}^n = \frac{\rho}{X^d}D_t^-u_{\text{in}}^{n+\frac{1}{2}}\mathbf{j}_{\text{in}} \,, \tag{35}$$

where here, $\mathbf{Q} = \sqrt{c/X^d}\mathbf{N}(\mathbf{SM})^{\frac{1}{2}}$. This is an extremely compact extension of the basic scheme (20); again, using Sherman-Morrison, the required linear system solution can be reduced to size $V \times V$. Such a form is useful in modeling rigid boundaries. The linear system to be solved is again strictly positive definite by construction—this desirable property follows directly from the adjoint approximations to the divergence and gradient, and also to the interpolants and forcing functions.

IV. NUMERICAL EXAMPLES

In this section, results are presented under different configurations of the immersed boundary in both 2D and 3D. In all cases, we set $\rho = 1.18$ kg·m^{-d} and $c = 344$ m·s^{-1}, and the time step is chosen as $T = 1/48000$ s (and the sample rate is SR $= 1/T$). The grid spacing X is chosen to satisfy the CFL condition $cT/X \leq 1/\sqrt{d}$ as close to equality as possible. Simulations are run over a cube-shaped region sufficiently large to contain the immersed boundary, and with first order absorbing boundary conditions[36] at the outer boundary. For plotting visibility, the driving function $u_{\text{in}}(t)$ (and its sampled discrete-time counterpart) is chosen here to be of the form of a doubly-differentiated Gaussian:

$$u_{\text{in}}(t) = \frac{2}{\sqrt{3\sigma_0}\pi^{1/4}}\left(1 - \frac{(t-t_0)^2}{\sigma_0^2}\right)e^{-(t-t_0)^2/2\sigma_0^2} \,. \tag{36}$$

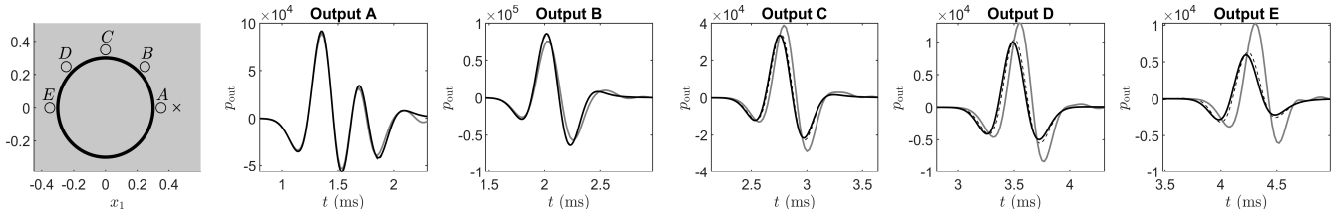

FIG. 5. Scattering from a rigid circular barrier. Left: configuration, with output locations A-E indicated by circles. and the source location by a cross. Right: output pressures generated by a staircased boundary (grey), an immersed boundary (dashed) as compared with the exact solution (solid line).

t_0 is chosen such that $u_{\text{in}}(0) = 1.1 \times 10^{-16}$, or machine epsilon in double precision floating point. One may also write $\sigma_0 = 1.321/f_0$, where f_0 is the frequency in Hz at which the spectral magnitude of u_{in} has decreased by 100 dB from its maximal value, defining an effective excitation bandwidth. For input and output at non-grid locations, bi(tri)cubic interpolation is employed.

It is also useful to define the nondimensional parameter $\theta = \Delta\sigma/X^{d-1}$, a measure of the density of forcing terms relative to the spatial grid; for the simulations presented here, $\Delta\sigma$, the $(d-1)$-dimensional patch area corresponding to a single forcing term on the immersed boundary, will be taken to be constant over all patches.

A. Circular Boundary in 2D

As a first example, consider exterior scattering of a point source from a rigid circular boundary in 2D (here of radius 30 cm), a case for which an exact solution is available[37]. Impedance condition (8) is used with a very high value of $M = 10^{11}$, corresponding to a Neumann condition, a relative density of forcing locations of $\theta = 1.2$, and bicubic interpolation. See Figure 5. Here, stringent conditions are used: a wideband pulse of the form of (36) is used, with an effective bandwidth $f_0 = 10$ kHz, and drives the wave equation at a location in close proximity to the circular barrier at $(45, 0)$ cm. Outputs are taken at locations near the barrier, at a radius of 35 cm. Staircasing leads to large deviations from the exact solution, particularly on the far side of the barrier, where coherence is disturbed and amplitudes are greatly overestimated. The immersed boundary performs much better, with some residual error due primarily to the numerical dispersion inherent to the scheme itself.

It is useful to examine the effect of the choice of interpolant on the behaviour of the immersed boundary, leading to major effects in terms of the coherence of computed responses. In Figure 6, responses for different orders of interpolant (nearest neighbour, bilinear and bicubic) are shown, for the same scenario as the previous example, at point E in Figure 5. Using a nearest neighbour interpolant, results are poor, and of comparable quality, in terms of coherence, to results obtained under staircasing, which is expected. Precursors are also visible in all cases, but are reduced in passing from bilinear to bicubic interpolation. The residual phase delay is due to the dispersion of the scheme itself under wideband excitation.

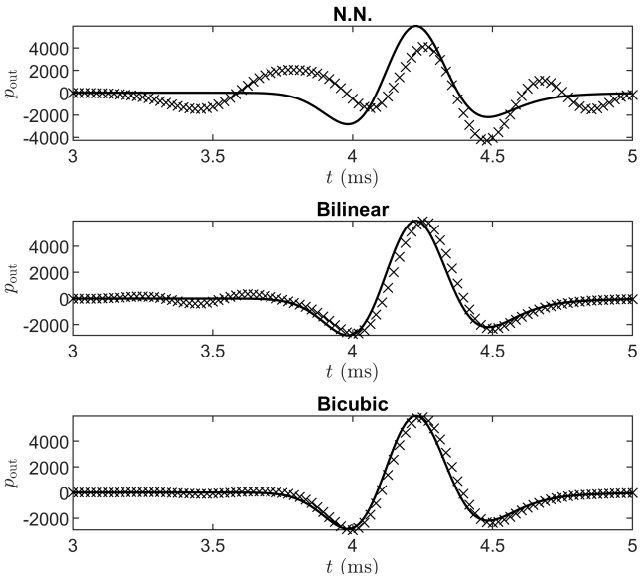

FIG. 6. Computed pressure outputs at point E as shown in Figure 5, for different choices of immersed boundary interpolant, as indicated. The exact solution is plotted as a solid line, and the FDTD solution as crosses.

To better illustrate the performance of the IB method relative to staircased boundary conditions, consider again the response at point E in Figure 5, now under refinement of the grid in the case of staircasing methods. In Figure 7, computed outputs are shown for IB and staircasing methods, both at the base sampling rate of SR = 48 kHz, and for staircasing at twice and four times the base sample rate. Convergence is slow for staircasing, with IB outperforming it at these rates. Comparable error for staircasing is achieved at a sample rate of approximately SR = 400 kHz. Given that, for volumetric simulation, memory requirements/operation counts scale as the third/fourth power of the sample rate, the IB method offers major advantages in this case.

As a concrete example, consider the present case of a simulation over a square region of side length 2.2 m, and

for a total simulation duration of 10 ms. Computation time for the IB method at the base rate of SR = 48 kHz, including the required linear system solution, is 1.6 s (Matlab, running on a standard laptop with an Intel i7). For a staircased termination, at an oversampled rate of SR = 400 kHz, the total simulation time is 869 s.

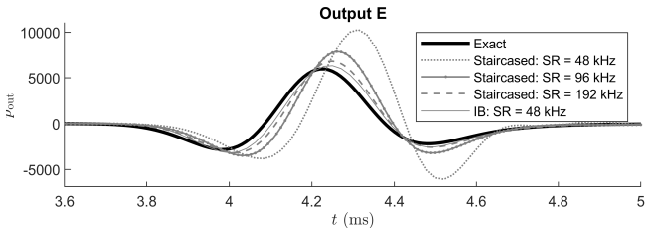

FIG. 7. Computed pressure outputs at point E as shown in Figure 5, for the immersed boundary method at a base rate of 48 kHz, and for a staircased termination at increased rates.

B. Square Boundary in 2D

As an example of an enclosed space, consider a square boundary, excited by a source in its interior. Again, a purely inertial immersed boundary boundary is used ($M = 10^{11}$) corresponding to a rigid boundary, for different rotations of the square relative to the underlying grid. See Figure 8. An elementary exact solution is available in this case through a modal expansion. The square is of side length 35 cm and centered at the origin, and the source and receiver locations are chosen, in unrotated coordinates, as $(10, 5)$ cm and $(-7, -2)$ cm, respectively. The input signal is again of the form (36) with $f_0 = 10$ kHz, and the relative forcing density is $\theta = 1.2$. Time domain responses under staircasing track the exact solution well when the square is aligned with the computational grid, but otherwise exhibit large deviations, even at very short time scales; similarly, spectral plots show sigificant errors in the placement of modal frequencies, and also significant variation under rotation. All such errors are greatly reduced in the immersed boundary results.

A major difficulty with immersed boundary methods is leakage through a boundary[38]; a problem which is absent under form-fitted meshing with a flux conservative method. It is important to distinguish here between leakage through a barrier intended to be airtight, and the physical phenomenon of transmission through a barrier; it is the former case that is of interest here. Spurious leakage is a complex phenomenon, with leakage depending on frequency, the type of interpolant used, as well as the relative density of forcing locations θ. To investigate this, consider a square of side length 2m, rotated at $\pi/6$ relative to the computational grid. In Figure 9, amplitude decay curves are shown for pressure signals p_{out} drawn from inside the square region, then RMS averaged. In general, spurious leakage increases with excitation bandwidth f_0, and decreases with the forcing point density θ, with good results obtained at about $\theta = 2$. Note that leakage is sensitive to the choice of θ (see Su et al.[22] for perspectives on the optimisation of θ). A bicubic interpolant is used here; not shown here are results for bilinear and nearest neighbour interpolants, which lead to larger spurious leakage in all cases. For a small enclosure such as this, leakage is on the order of 1-3 dB per second; not large, but significant in the setting of virtual acoustics. But, from geometric considerations, as the enclosure size is increased, the rate of spurious loss will decrease.

C. Spherical Boundary in 3D

Exterior scattering from a spherical boundary in 3D is a useful test problem, particularly in studies of head-related transfer functions[39]. Exact solutions are available in the case of scattering of a monopole point source from a rigid sphere[37]. A new difficulty, relative to the case of the circle in 2D, is the need for a regular sampling of the sphere. Here, a spiral-based sampling method[40] is used.

First consider the scenario of the scattering of a monopole source from a rigid sphere, generalizing the case of the circle described in Section IV A. Again, a source with effective bandwidth $f_0 = 10$ kHz is used, and an inertial immersed boundary with $M = 10^{11}$, $\theta = 1.5$ and tricubic interpolation is used. The sphere is of radius 25 cm, the source location is 40 cm distant from the sphere center, and outputs are drawn from five locations 30 cm distant from the sphere center. Comparisons between scattered outputs using staircasing and the immersed boundary are as shown in Figure 10. As before, the immersed boundary method solution tracks the exact solution very closely, even on the far side of the sphere.

As an example of the behaviour of the immersed boundary under more general impedance conditions, see Figure 11, showing the time evolution of the acoustic field of a spherical barrier in response to a point source, of effective bandwidth $f_0 = 8$ kHz. Here, the series impedance form (8) is used, in the case of a resistive barrier, and a barrier with both inertia and stiffness. In both cases, there is the expected penetration of wave propagation into the interior of the spherical barrier.

As a final demonstration, consider a spherical immersed boundary, again under the impedance condition (8), but with $R = 0$, so the condition itself is lossless. Under these conditions, a discrete-time energy balance of the form (34) will be satisfied, to near machine accuracy in double precision floating point arithmetic. See Figure 12, showing the partition of energy between the energy stored in the acoustic field, and the stored energy at the boundary due to inertial and stiffness effects. In this case, the input forcing function u_{in} is a simple unit impulse, and the outer conditions of the computational region $\mathcal{B}$ are chosen to be of lossless Neumann type. Also shown is the relative error in the computed energy, which fluctuates at approximately 10^{-14} of the total energy. This structural losslessness property, in conjunction with the CFL condition serves as a numerical stability condition. See Appendix A for a more general perspective on passivity and numerical stability.

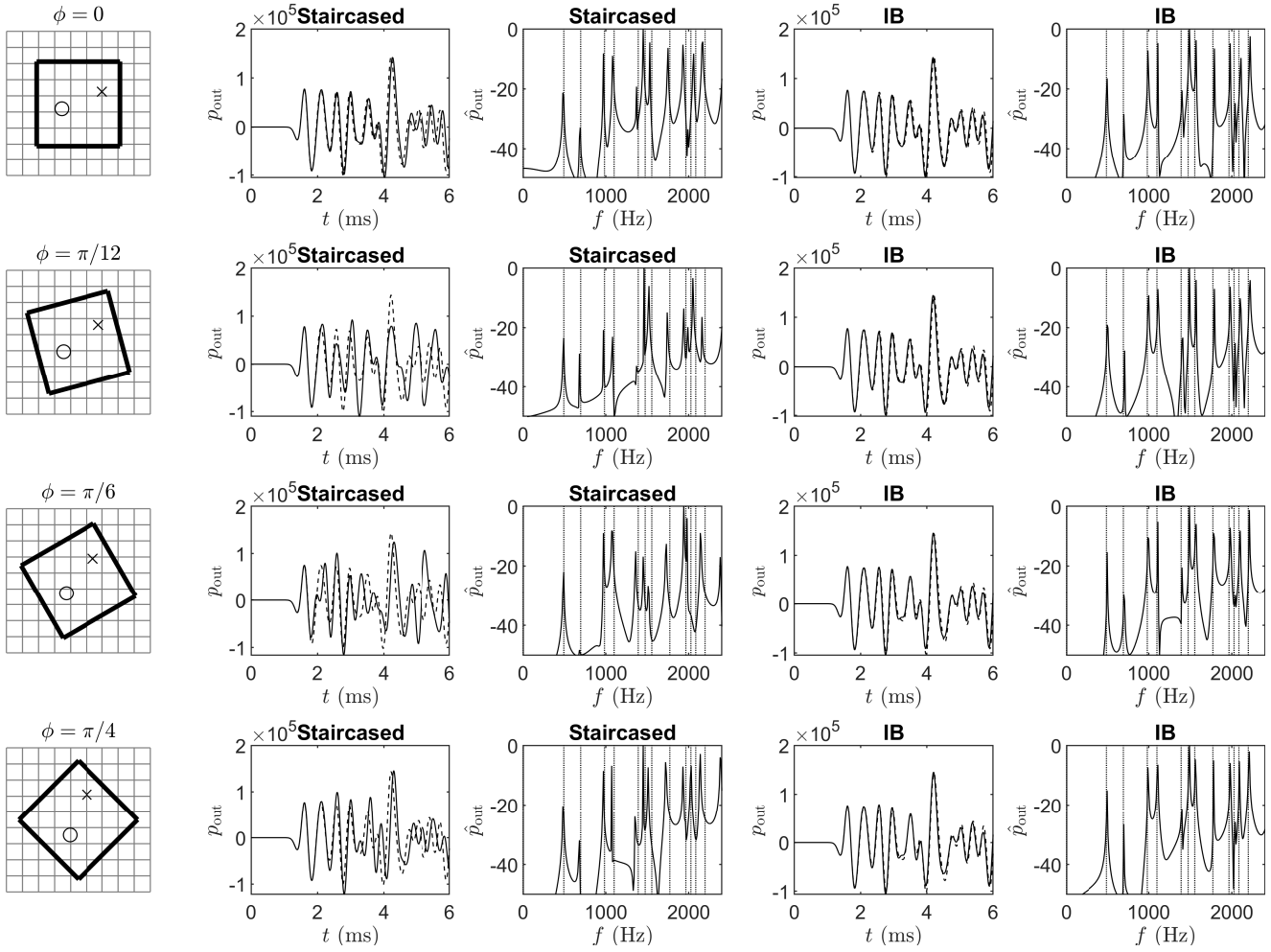

FIG. 8. Rotations of a square boundary relative to the computational grid, as illustrated at left for different angles of rotation ϕ as indicated. The time domain response p_{out} and its transform $\hat{p}_{\text{out}}$ are shown in the case of a staircased boundary in columns 2 and 3, and in the case of an immersed boundary in columns 4 and 5. For time domain responses, the exact solution is shown as a solid line, and FDTD solutions as a dashed line. For spectral plots, exact modal frequencies are indicated as vertical dotted lines. The total simulation duration is 0.1 s, and output signals are Hann-windowed before Fourier transformation.

V. CONCLUDING REMARKS

The focus of this article has been on the specialisation of immersed boundary method to numerical simulation techniques for the acoustic wave equation. One result of this specialisation is that it is possible to arrive at conclusive proofs of numerical stability, hinging on the key concept of numerical passivity (see Appendix A). Furthermore, the method proposed here can be employed directly within the simplest variety of FDTD without any further stability analysis required. The same ideas extend to any numerical simulation method that can be posed as in (30a)–(30d); that is, provided the discrete gradient and divergence operations are defined as adjoints. The extension to the case of FDTD schemes, or other simulation methods defined over regular grids, defined directly in terms of the second order wave equation[12] (which are generally preferable, due to reduced computational requirements) is more difficult, and has not been addressed here, and forms the basis for future work. In at least one special case shown here in (35), the immersed boundary may be included directly within a scheme for the second order wave equation.

The main additional computational cost is the requirement of a linear system solution over the set of boundary locations, which will be small relative to the size of the interior computational FDTD grid, over which the simple algorithm here remains fully explicit. Computational cost scaling thus bears some superficial resemblance to boundary element approaches[41], but here the linear system is rudimentary to compute (via, e.g., polynomial interpolants) and extremely sparse, with $O(V)$ non-zero values with additional dependency on interpolation width and the density of forcing locations. Not explored here are possibilities for the use of fast sparse linear system solution techniques[42].

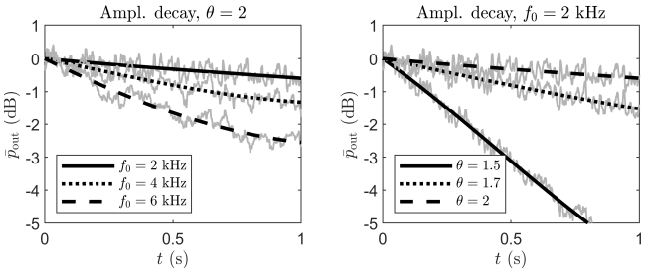

FIG. 9. RMS-averaged (over a 100 ms window) amplitude decay curves $\bar{p}_{\text{out}}$, for a square enclosure of side length 2m, rotated at $\pi/6$ with respect to the computational grid. Polynomial fits are shown, for better visibility. Results are shown, at left, for different effective bandwidths f_0, for a fixed value of $\theta = 2$, and at right for different values of θ, for a fixed effective bandwidth $f_0 = 2$ kHz.

In terms of performance in the context of virtual acoustics, for exterior scattering problems, immersed boundary methods clearly yield results far superior to staircased boundary methods, in terms of the coherence of scattered waves. An obvious application is to the numerical determination of head-related transfer functions, where immersed boundary methods permit operation over a relatively coarse numerical grid, even if there are complex features requiring sub-grid resolution[43] (requiring fine-grained staircasing, or relatively complex conformal meshing). For interior problems with rigid boundaries, however, the situation is less clear—over short time scales, there is the same coherence observed as in the exterior case, but over longer time scales, there are leakage effects that are nontrivial, which will impact upon decay times. As the immersed boundary as proposed here is a two-sided barrier, and intended to allow the transmission of energy, this is expected (though as shown here, the Neumann condition may be modelled here through the choice of a high-mass inertial condition). For the modeling of enclosures with impedance conditions, techniques such as blanking of exterior cells[44], or sharp interface methods[10] could be considered. The relationship between point forcing density, frequency and the type of interpolant on such leakage remains an open question, but some preliminary perspectives appear in Section IV B.

APPENDIX A: NUMERICAL STABILITY

The passivity property of the impedances ζ, when discretized using the trapezoid rule, and in conjunction with the simple FDTD scheme presented here leads immediately to simple conditions for numerical stability. The immersed boundary design does not interfere with this analysis, and the normal CFL condition may be employed. If a concrete realisation of the impedances is available, dissipativity or losslessness may be demonstrated directly in the time domain, as in Section IIIG; even without such a realisation, the passivity property persists, and may be used to show numerical stability for the complete update using Laplace techniques, as illustrated below. The analysis here is related to the case of impedance boundary conditions for FVTD methods[34] and is presented in condensed form here.

Consider the complete update as expressed in (30a)–(30d). The eigenfunctions are exponential solutions $\mathbf{w}^n = \hat{\mathbf{w}} e^{s_d n T}$, where here, $s_d = \sigma_d + j\omega_d$ is a discrete complex frequency variable, with $\pi/T < \omega_d \leq \pi/T$, and $\hat{\mathbf{w}}$ is a complex amplitude. $\mathbf{w}$ here could represent any of the components $\mathbf{p}$, $\mathbf{v}$, $\mathbf{p}^*$ or $\mathbf{v}^*$. The object here is to find a stability condition under which the update does not permit exponentially-growing solutions with $\sigma_d > 0$.

For such solutions, the discrete-time operators from (15), (16), and (27) behave as multiplicative factors:

$$D_t^{\pm} \to e^{\pm s_d T/2}\alpha \qquad \alpha = \frac{2}{T}\sinh(s_d T/2) \quad \text{(A1a)}$$

$$D_t^{\circ} \to \beta \qquad \beta = \frac{2}{T}\tanh(s_d T/2) \quad \text{(A1b)}$$

$$\mu_t^{-} \to e^{-s_d T/2} m \qquad m = \cosh(s_d T/2). \quad \text{(A1c)}$$

In particular, under trapezoidal integration, positive real functions in s are mapped to positive real functions in s_d. So, for the impedances $\zeta_\nu(s)$, $\nu = 1, \ldots, V$:

$$\text{Re}(\zeta_\nu(\beta)) \geq 0 \qquad \text{when} \qquad \text{Re}(s_d) > 0. \quad \text{(A2)}$$

Let the $V \times V$ matrix $\mathbf{Z}(\beta)$ contain the impedances $\zeta_\nu(\beta)$, $\nu = 1, \ldots, V$ on the diagonal. Using (30c),

$$\hat{\mathbf{p}}^* = -Z_0 \mathbf{Z}(\beta)\hat{\mathbf{v}}^* = -Z_0 \mathbf{Z}(\beta)\mathbf{N}^T\hat{\mathbf{v}}. \quad \text{(A3)}$$

Combining this with (30a) and (30b) and simplifying leads to a matrix form for exponential solutions to the update at discrete frequency s_d:

$$\underbrace{\begin{bmatrix} \frac{\alpha}{\rho c^2}\mathbf{I}_{N_p} & \mathbf{D} \\ -\frac{1}{m}\mathbf{D}^T & \rho\beta\mathbf{I}_{N_v} + \mathbf{G}\mathbf{Z}(\beta)\mathbf{G}^T \end{bmatrix}}_{\mathbf{H}(s_d)} \begin{bmatrix} \hat{\mathbf{p}} \\ \hat{\mathbf{v}} \end{bmatrix} = \begin{bmatrix} \frac{\hat{u}_{\text{in}}}{X^d}\mathbf{j}_{\text{in}} \\ \mathbf{0} \end{bmatrix} \quad \text{(A4)}$$

where here, $\hat{u}_{\text{in}}$ is the complex amplitude of the source signal at frequency s_d, and where $\mathbf{G} = \sqrt{Z_0/X^d}\mathbf{N}\mathbf{S}^{1/2}$.

Suppose now that there is a nontrivial solution to (A4) at a frequency $s_d = \bar{s}_d$ with $\bar{\sigma}_d > 0$. This implies that $\det(\mathbf{H}(\bar{s}_d)) = 0$, and further that $\det(\mathbf{H}_{11}(\bar{s}_d))\det(\mathbf{H}_{11}^{\dagger}(\bar{s}_d)) = 0$, where $\mathbf{H}_{11}$ is the upper left-hand block of $\mathbf{H}$, and $\mathbf{H}_{11}^{\dagger}$ is its Schur complement. Clearly $\alpha \neq 0$ for $s_d = \bar{s}_d$, so $\mathbf{H}_{11}$ is nonsingular. Using $\bar{\alpha} = \alpha(\bar{s}_d)$, $\bar{\beta} = \beta(\bar{s}_d)$ and $\bar{m} = m(\bar{s}_d)$ we have:

$$\mathbf{H}_{11}^{\dagger} = \rho\bar{\beta}\mathbf{I}_{N_v} + \mathbf{G}\mathbf{Z}(\bar{\beta})\mathbf{G}^T + \frac{\rho c^2}{\bar{\alpha}\bar{m}}\mathbf{D}^T\mathbf{D}. \quad \text{(A5)}$$

For the determinant of $\mathbf{H}_{11}^{\dagger}$ to vanish, it must be true that there is a non-zero vector $\mathbf{r}$ such that $\mathbf{r}^T\mathbf{H}_{11}^{\dagger}(\bar{s}_d)\mathbf{r} = 0$. But, using the positive realness property of the diagonal elements of $\mathbf{Z}$, from (A2), we have

$$\text{Re}(\mathbf{r}^T\mathbf{H}_{11}^{\dagger}\mathbf{r}) \geq \rho\text{Re}\left(\bar{\beta}|\mathbf{r}|^2 + \frac{c^2}{\bar{\alpha}\bar{m}}|\mathbf{D}\mathbf{r}|^2\right). \quad \text{(A6)}$$

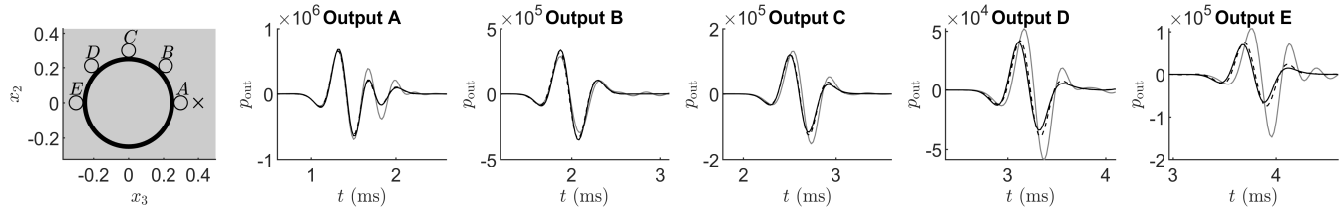

FIG. 10. Scattering from a rigid spherical barrier. Left: configuration, with output locations A-E indicated by circles. and the source location by a cross. Right: output pressures generated by a staircased boundary (grey), an immersed boundary (dashed) as compared with the exact solution (solid line).

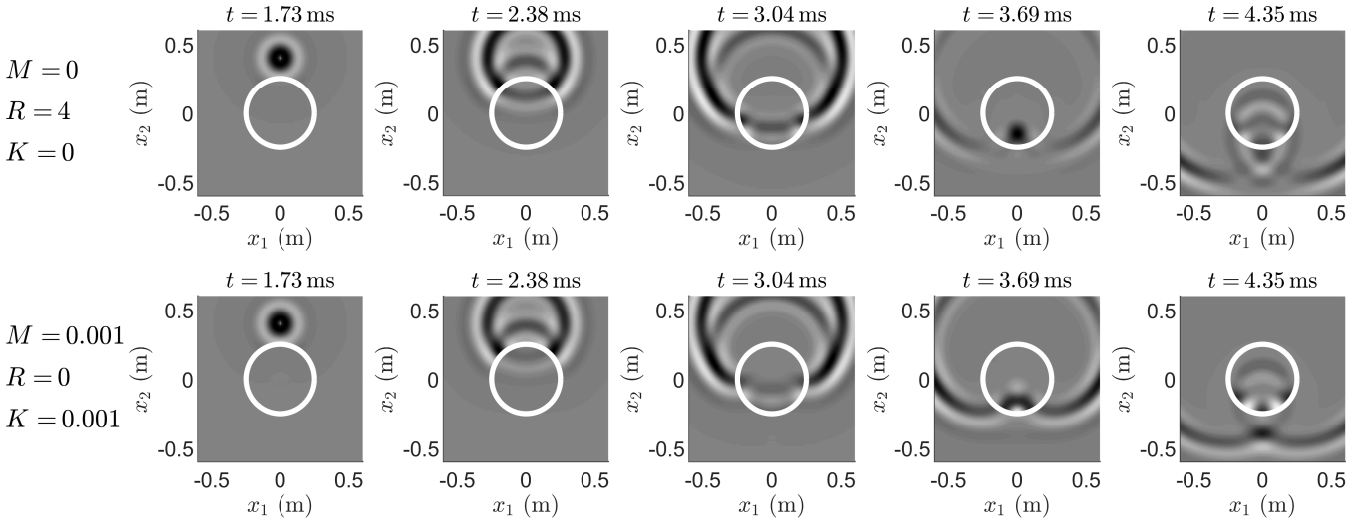

FIG. 11. Time evolution of the acoustic field of a monopole source scattered from a spherical boundary under impedance condition (8), with parameters M, R and K as indicated. The cross-section in the (x_1, x_2) plane is shown, and the source is located at $x_1 = 0$, $x_2 = 0.4$ m. Top row: a resistive barrier, and bottom row: a lossless barrier with inertia and stiffness.

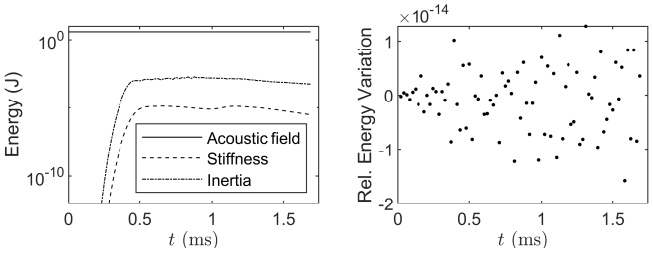

FIG. 12. Discrete energy conservation for a spherical immersed boundary ($M = 0.001$, $K = 1000$). Left: energy partition as a function of time, showing energy contained in the acoustic field, and the stiffness and inertia of the barrier. Right: the relative variation in the discrete energy $\mathcal{E} = \mathcal{E}_{\text{ac}} + \mathcal{E}_{\text{b}}$, as given in (34), and defined as $(\mathcal{E}^{n+1/2} - \mathcal{E}^{1/2})/\mathcal{E}^{1/2}$.

Furthermore, because[34]

$$\text{Re}\left(\bar{\beta}\right) > 0 \qquad \text{and} \qquad \text{Re}\left(\frac{1}{\bar{\alpha}\bar{m}}\right) \geq -\frac{T^2}{4}\text{Re}\left(\bar{\beta}\right), \tag{A7}$$

we have

$$\begin{aligned}\text{Re}(\mathbf{r}^T\mathbf{H}_{11}^{\dagger}\mathbf{r}) &\geq \rho\text{Re}\left(\bar{\beta}\right)\left(|\mathbf{r}|^2 - \frac{c^2T^2}{4}|\mathbf{D}\mathbf{r}|^2\right) \\ &\geq \rho\text{Re}\left(\bar{\beta}\right)\left(1 - \frac{c^2T^2}{4}\lambda_{\max}\right)|\mathbf{r}|^2,\end{aligned} \tag{A8}$$

where $\lambda_{\max}$ is the maximum eigenvalue of $\mathbf{D}^T\mathbf{D}$. For the basic spatial difference approximations to the gradient and divergence employed here, we have $\lambda_{\max} = 4d/X^2$. This implies finally, that $\mathbf{H}_{11}^{\dagger}$ is nonsingular, and thus that no solutions exist with $\sigma_d > 0$, under the condition

$$cT/X \leq \sqrt{1/d}. \tag{A9}$$

Thus the conventional CFL bound for the nearest neighbour scheme for the wave equation in d dimensions[11] has been recovered. Notice that the presence of the immersed boundary has no effect on this stability condition; this is due to the particular discretisation strategy used for the immersed boundary impedances (notably the passivity-preserving trapezoid rule).

[1]L. Savioja, T. Rinne, and T. Takala, "Simulation of room acoustics with a 3-D finite-difference mesh," in *Proc. Int. Comp. Music Conf.*, Århus, Denmark (1994), pp. 463–466.

[2]D. Botteldooren, "Finite-difference time-domain simulation of low-frequency room acoustic problems," J. Acoust. Soc. Am. **98**(6), 3302–3308 (1995).

[3]K. Kowalczyk and M. van Walstijn, "Room acoustics simulation using 3-D compact explicit FDTD schemes," IEEE Trans. Audio, Speech, Lang. Process. **19**(1), 34–46 (2011).

[4]S. Bilbao, B. Hamilton, J. Botts, and L. Savioja, "Finite volume time domain room acoustics simulation under general impedance boundary conditions," IEEE/ACM Trans. Audio, Speech, Lang. Process. **24**(1), 161–173 (2016).

[5]M. Hornikx, W. De Roeck, and W. Desmet, "A multi-domain Fourier pseudospectral time-domain method for the linearized Euler equations," J. Comp. Phys. **231**(14), 4759–4774 (2012).

[6]R. Mehra, N. Raghuvanshi, L. Savioja, M. Lin, and D. Manocha, "An efficient GPU-based time domain solver for the acoustic wave equation," Appl. Acoust. **73**(2), 83–94 (2012).

[7]F. Pind, A. Engsig-Karup, C. Jeong, J. Hesthaven, M. Mejling, and J. Stromann-Andersen, "Time domain room acoustic simulations using the spectral element method," J. Acoust. Soc. Am. **145**(6), 3299–3310 (2019).

[8]H. Wang, I. Sihar, R. Munoz, and M. Hornikx, "Room acoustics modelling in the time-domain with the nodal discontinuous Galerkin method," J. Acoust. Soc. Am. **145**(4), 2650–2663 (2019).

[9]B. Hamilton, C. J. Webb, N. D. Fletcher, and S. Bilbao, "Finite difference room acoustics simulation with general impedance boundaries and viscothermal losses in air: Parallel implementation on multiple GPUs," in *Proc. Int. Symp. Music & Room Acoust.*, Buenos Aires, Argentina (2016).

[10]C. Brehm and H. Fasel, "A novel concept for the design of immersed interface methods," J. Comp. Phys. **242**, 234–267 (2013).

[11]R. Courant, K. Friedrichs, and H. Lewy, "On the partial differential equations of mathematical physics," Mathematische Annalen **100**, 32–74 (1928).

[12]S. Bilbao and B. Hamilton, "Higher-order accurate two-step finite difference schemes for the many-dimensional wave equation," J. Comput. Phys. **367**, 134–165 (2018).

[13]R. Leveque, *Finite Volume Methods for Hyperbolic Problems* (Cambridge University Press, Cambridge, UK, 2002).

[14]M. Popescu, R. Vedder, and W. Shyy, "A finite volume-based high-order, Cartesian cut-cell method for wave propagation," Int. J. Num. Meth. Fluids **56**, 1787–1818 (2008).

[15]M. Berger and A. Giuliani, "A state redistribution algorithm for finite volume schemes on cut cell meshes," J. Comp. Phys. **428**, 1–20 (2021).

[16]C. Peskin, "Flow patterns around heart valves: A numerical method," J. Comp. Phys. **10**, 252–271 (1972).

[17]D. Goldstein, R. Handler, and L. Sirovich, "Modeling a no-slip flow boundary with an external force field," J. Comp. Phys. **105**, 354–366 (1993).

[18]R. Mittal and G. Iaccarino, "Immersed boundary methods," Ann. Rev. Fluid Mech. **37**, 239–261 (2005).

[19]W. Huang and F. Tian, "Recent trends and progress in the immersed boundary methods," J. Mech. Eng. Sci. **233**, 7617–7636 (2019).

[20]R. Komatsu, W. Iwakami, and Y. Hattori, "Direct numerical simulation of aeroacoustic sound by volume penalization method," Computers and Fluids **130**, 24–36 (2016).

[21]A. Bhalla, R. Bale, B. Griffith, and N. Patankar, "A unified mathematical framework and an adaptive numerical method for fluid-structure interaction with rigid, deforming and elastic bodies," J. Comp. Phys. **250**, 446–476 (2013).

[22]S. Su, M. Lai, and C. Lin, "An immersed boundary technique for simulating complex flows with rigid boundary," Comp. and Fluids **36**, 313–324 (2007).

[23]J. Seo and R. Mittal, "A high-order immersed boundary method for acoustic wave scattering and low-Mach number flow-induced sound in complex geometries," J. Comp. Phys. **230**(4), 1000–1019 (2011).

[24]X. Sun, Y. Jiang, A. Liang, and X. Jing, "An immersed boundary computational model for acoustic scattering problems with complex geometries," J. Acoust. Soc. Am. **132**(5), 3190–3199 (2012).

[25]L. Wang, F.-B. Tian, and J. Lai, "An immersed boundary method for fluid–structure–acoustics interactions involving large deformations and complex geometries," J. Fluids Structures **95**, 1–27 (2020).

[26]D. Takeuchi, K. Yatabe, and Y. Oikawa, "Source directivity approximation for finite-difference time-domain simulation by estimating initial value," J. Acoust. Soc. Am. **145**(4), 2638–2649 (2019).

[27]S. Bilbao, J. Ahrens, and B. Hamilton, "Incorporating source directivity in wave-based virtual acoustics: Time-domain models and fitting to measured data," J. Acoust. Soc. Am. **146**(4), 2692–2703 (2019).

[28]B. Anderson and S. Vongpanitlerd, *Network Analysis and Synthesis* (Prentice-Hall, Englewood Cliffs, New Jersey, 1973), p. 51.

[29]K. Yee, "Numerical solution of initial boundary value problems involving Maxwell's equations in isotropic media," IEEE Trans. Antennas Prop. **14**, 302–307 (1966).

[30]J. Tuomela, "On the construction of arbitrary order schemes for the many-dimensional wave equation," BIT **36**(1), 158–165 (1996).

[31]Y. Liu and Y. Mori, "Properties of discrete delta functions and local convergence of the immersed boundary method," SIAM J. Numer. Anal. **50**(6), 2986–3015 (2012).

[32]B. Hosseini, N. Nigam, and J. Stockie, "On regularizations of the Dirac delta distribution," J. Comp. Phys. **305**, 423–447 (2016).

[33]S. Bilbao, "3D interpolation in wave-based acoustic simulation," IEEE Signal Proces. Lett. **29**, 384–387 (2021).

[34]S. Bilbao and B. Hamilton, "Passive volumetric time domain simulation for room acoustics applications," J. Acoust. Soc. Am. **145**(4), 2613–2624 (2019).

[35]R. Horn and C. Johnson, *Matrix Analysis* (Cambridge University Press, Cambridge, UK, 2012), p. 19.

[36]B. Engquist and A. Majda, "Absorbing boundary conditions for the numerical evaluation of waves," Math. Comp. **31**(139), 629–651 (1997).

[37]J. Hao, F. Perot, R. Kotapati, and A. Mann, "Numerical studies of acoustic diffraction by rigid bodies," in *Proc. 22nd AIAA/CEAS Aeroacoustics Conf.*, Lyon, France (2016).

[38]B. Kallemov, A. Bhalla, B. Griffith, and A. Donev, "An immersed boundary method for rigid bodies," Comm. Appl. Math. Comp. Sci. **11**(1), 79–141 (2016).

[39]R. Duda and W. Martens, "Range dependence of a spherical head model," J. Acoust. Soc. Am. **104**(5), 3048–3058 (1998).

[40]C. Koay, "Analytically exact spiral scheme for generating uniformly distributed points on the unit sphere," J. Comp. Sci. **2**(1), 88–91 (2011).

[41]S. Kirkup, "The boundary element method in acoustics," Applied Sciences **9**(8), 1–50 (2019).

[42]Y. Saad, *Iterative Methods for Sparse Linear Systems*, 2nd ed. (SIAM, Philadelphia, 2003).

[43]S. Prepeliță, M. Geronazzo, F. Avanzini, and L. Savioja, "Influence of voxelization on finite difference time domain simulations of head-related transfer functions," J. Acoust. Soc. Am. **139**(5), 2489–2504 (2016).

[44]S. Péron, C. Benoit, T. Renaud, and I. Mary, "An immersed boundary method on Cartesian adaptive grids for the simulation of compressible flows around arbitrary geometries," Engineering with Computers **37**, 2419–2437 (2020).